3D Reconstruction of Super-Resolved Micro-CT Images of Kaolinite-filled Sandstones

Pit Arnold[1,*], *Viswambhar Reddy* Yasa[1], *Mayank* Nagar[1], *Till* Bollermann[1], *Mohsen* Rafiee[2], *Wesam* Ben Mansour[2], and *Andrew* Fogden[1]

[1]Harbour Energy, Technology and Service Center, 49406 Barnstorf, Germany
[2]Harbour Energy, Jåttåflaten 27, 4020 Stavanger, Norway

Abstract. For digital core analysis of reservoir sandstones, the 3D images of internal pore structure for simulation are typically provided by micro-CT. This standard workflow becomes insufficient for samples of low permeability or wide distribution of pore sizes contributing to flow, demanding a multiscale strategy incorporating higher-resolution 3D images of microporosity. This paper presents a readily implementable methodology, building on recent machine-learning and GAN-based super-resolution approaches, to generate realistic 3D rock micro-models by combining micro-CT images with SEM 2D images of embedded polished sections. Our archive comprises hundreds of these images from Norwegian Continental Shelf sandstones, providing the basis for training of CycleGAN models on unpaired image crops, with particular focus on kaolinite-hosted microporosity. The trained models transformed these microporous regions from poorly-resolved micro-CT into super-resolution 3D cubes, through slice generation, interpolation, alignment and recombination. In this way, 39 realistic kaolinite-microstructural cubes of 1000-voxel at 0.15 µm voxel size were generated, spanning porosities of 11–56% and absolute permeabilities of 0.3–120 mD, on which gas-water relative permeability and capillary pressure curves were simulated. The application of these microstructures and properties to digital core analysis with machine learning-augmentation was illustrated by a case study of low permeability kaolinite-rich sandstones from a gas reservoir.

1 Introduction

A variety of laboratory techniques exist for rock imaging, differing in their principle and modality, investigation depth, spatial resolution and field of view, as well as sample preparation requirements [1,2]. X-ray computed tomography CT generates 3D images of internal structure from whole core to core plugs using medical/industrial CT, and plugs to subsamples using micro-CT. Polarized-light microscopy of optical thin sections and scanning electron microscopy (SEM) of rough surfaces or planar embedded sections are common analytical 2D imaging techniques. Geological description combines these techniques to cover a broad range of length scales, and can be complemented by digital post-processing tools for paired image comparison.

Fluid flow is governed by the network of pore bodies and their connecting pore throats, for which the sizes relevant to hydrocarbon recovery from conventional reservoir rocks or CO_2 storage can range from 10 nm to 1 mm in core plugs. Use of digital core analysis (DCA) to simulate flow properties requires 3D images encompassing representative volumes while also resolving the smallest throats of significance [3,4]. Micro-CT 3D imaging of a plug subsample for segmentation of resolved pore space, in which two-phase flow processes are simulated, is common practice [5] and referred to here as the standard DCA methodology. This single-scale approach is well-suited to relatively clean, homogeneous sandstones of sufficiently high permeability. It becomes increasingly problematic though for tighter or more heterogeneous samples, as shown in the example of Fig. 1a-b, given that micro-CT is practically limited to image width maximum of 3000 voxels and voxel size minimum of 0.5 µm [6]. SEM imaging of polished sections using backscattered electrons (BSE) offers much greater range of width and resolution, as shown in the example of Fig. 1c, with the added modality of mineral mapping by energy-dispersive x-ray spectroscopy EDS [7]. However, two-phase flow cannot be simulated realistically on these 2D images, and for the 2D-3D hybrid technique of focused ion beam FIB-SEM, the image stacks are typically too small for conventional reservoir rocks.

To overcome the limitations of this trade-off between micro-CT field of view and resolution demands a multiscale approach, in which the macro-pore space resolved by micro-CT is complemented by alternative technologies to generate realistic 3D models of rock microporosity. Moreover, flow in these macro- and micro-pore networks must be coupled by development of multiscale simulation tools [8-10].

* Corresponding author: pit.arnold@harbourenergy.com

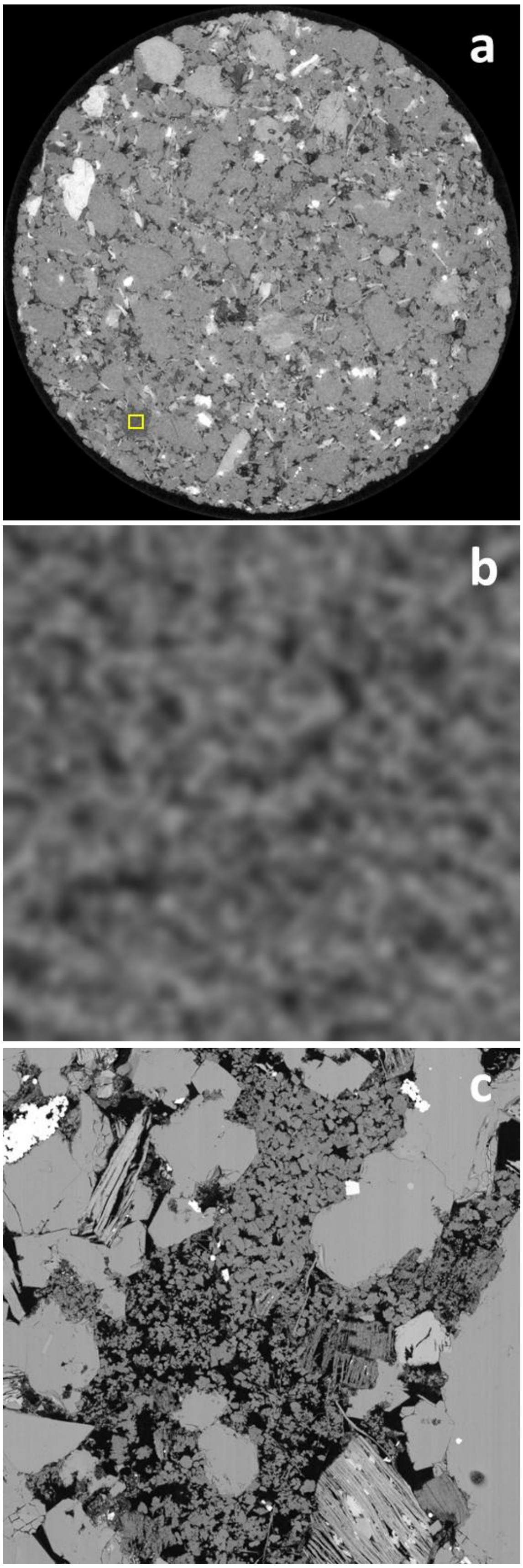

Fig. 1. Rock images from sandstone core plug *E*. a) cross-sectional slice of high-resolution micro-CT 3D image of subsample: 5.7 × 5.7 mm, voxel size 2.33 µm; b) cube cropped from kaolinite-filled pore (yellow box in a): 0.15 × 0.15 mm, voxel size 2.33 µm; c) SEM 2D image from polished section: 0.44 × 0.51 mm, pixel size 0.25 µm.

Further progress in these objectives would greatly benefit the dynamic modelling of gas and gas-condensate in conventional reservoir sandstones of permeability range 0.1-1 mD, for which SCAL experiments can be time-consuming, costly and error-prone. In such rocks, the inter-granular microporosity relevant to hydrocarbon flow is often hosted by booklet aggregates of kaolinite (e.g., Fig. 1c), while other clay minerals such as illite are often associated with tighter micropores, remaining largely brine-filled.

Digital construction of 3D rock microstructures began with process-based or stochastic modelling [11,12], and has greatly advanced over recent years by harnessing the developments in machine learning (ML) [13,14]. These ML approaches have tackled the two related challenges of reconstructing 3D pore structures from limited 2D information and enhancing low-resolution images. Foundational studies demonstrated that meaningful 3D porous media could be generated from training volumes using the architecture of Generative Adversarial Networks (GAN), while later work moved toward true sparse-input reconstruction from 2D slices or other limited conditioning data [15-18]. In parallel, digital-rock super-resolution technology evolved from paired Convolutional Neural Networks (CNN) approaches trained on synthetic degradations to physically-grounded paired and unpaired methods trained on real multi-resolution or unregistered micro-CT data [19-25].

The ML approach of the current paper uses our large archive of unpaired micro-CT 3D and SEM 2D images of Norwegian Continental Shelf (NCS) reservoir sandstones to train CycleGAN models, enabling a super-resolution reconstruction of microporous regions, primarily hosted by kaolinite. These were sufficiently realistic and artifact-free for use in two-phase flow simulations. From the resulting set of SEM-like 3D cubes, their microscale-simulated flow properties were combined and upscaled to the micro-CT images using a ML-augmented DCA methodology, which was illustrated using a case study of core plugs from one NCS gas reservoir well.

2 Methodology

2.1. Generative Adversarial Networks (GAN)

GAN use generative and discriminative models in a competitive framework, where both networks are trained simultaneously [26]. The objective is to generate data that can no longer be distinguished from real data, providing image models with a way to learn “realism” directly from data without pixel-by-pixel comparisons. Later, Deep Convolutional GAN (DCGAN) introduced an architectural improvement by replacing fully-connected layers with deep convolutional networks, leading to significantly enhanced performance in unsupervised learning and improved stability during image generation [27]. These developments laid the foundation for the CylceGAN used in the current study [28].

2.2. Cycle Generative Adversarial Networks (CycleGAN)

CycleGAN, in its standard form, uses two generators and two discriminators. One generator translates images from a source-domain into target-domain-like images, while the second generator learns the inverse mapping. Adversarial losses encourage outputs that resemble real sample images from the target domain, while the cycle-consistency loss preserves structural information by penalizing discrepancies after a round-trip translation [28]. This enables image-to-image translation while maintaining important structural features.

Training data for the current study came from the large archive of NCS reservoir sandstone images accumulated by our Digital Rocks lab over the past six years. This archive contains hundreds of high-resolution micro-CT 3D images of plug subsamples, together with corresponding SEM 2D images and mineral maps of polished sections from the same plug. A major advantage of CycleGAN is that it supports unpaired image-to-image translation, making it particularly suitable for this study, since paired micro-CT and SEM images are scarce in our archive.

For training, a subset of plug images from various NCS fields, wells and formations was selected, focusing on kaolinite-rich samples having high-resolution micro-CT images with voxel size of approximately 2 µm (e.g., Fig. 1a). From these volumes, a multitude of 2D squares containing poorly-resolved kaolinite-rich microporosity (e.g., Fig. 1b) were cropped, providing a sufficiently large source-domain dataset for model training. In parallel, the SEM BSE 2D images (all of 0.25 µm pixel size, e.g. Fig. 1c), capturing at detailed resolution the variable size, morphology and spatial arrangement of kaolinite booklet aggregates, were similarly used to crop a multitude of squares. The combination of both unpaired large datasets significantly reduced the uncertainty associated with training on sparse image information. It allowed the CycleGAN model to learn a representative transformation between the micro-CT and SEM expressions of kaolinite-rich regions.

In this study, two separate CycleGAN models were used, namely one for the image transformation and super-resolution generation, and later a second one for style refinement. In the first model, with flowchart illustrated in Fig. 2, our domain X consisted of the real 64×64 voxel squares from the micro-CT image set, while domain Y comprised the real 1024×1024 pixel squares from the SEM image set. Two GAN networks were used within the CylceGAN framework: GAN_1 translates micro-CT images to SEM-like images, while GAN_2 performs the inverse translation. Both generators are constrained by the cycle-consistency loss, which measures the difference between the original input image and the reconstructed image (i.e., GAN_1 followed by GAN_2, and vice-versa). One complete pass through the datasets of each domain, where each image is processed once, is referred to as an epoch. During training, the models parameters are updated iteratively, progressively reducing the discrepancy between real and synthetically-generated data. Each domain contained thousands of images, which were processed in batches over hundreds of epochs, to train a CycleGAN model effectively.

In the second CycleGAN model, the overall architecture and training procedure remained the same, however the content of the domains X and Y differed. In the first model, the purpose was image transformation and super-resolution, hence image regions containing kaolinite structures plus framework grains were used for training. In contrast, the second model focused primarily on style refinement. The input to its GAN_1 consisted of the 1024×1024 pixel slices of the combined output volumes (1024 cubes) generated by application of the first CycleGAN model and image post-processing, hence the resolution of domains X and Y was the same. Additionally, the SEM dataset Y for the second model was extended with further 1024×1024 pixel images, containing predominantly kaolinite structures without grains, to further improve the style transfer, as grains were also absent from the domain X dataset. The training of both CycleGAN models used a NVIDIA L40 GPU (48 GB) and were run in multiple cycles, with the final results using a pre-trained model from earlier trainings as starting point.

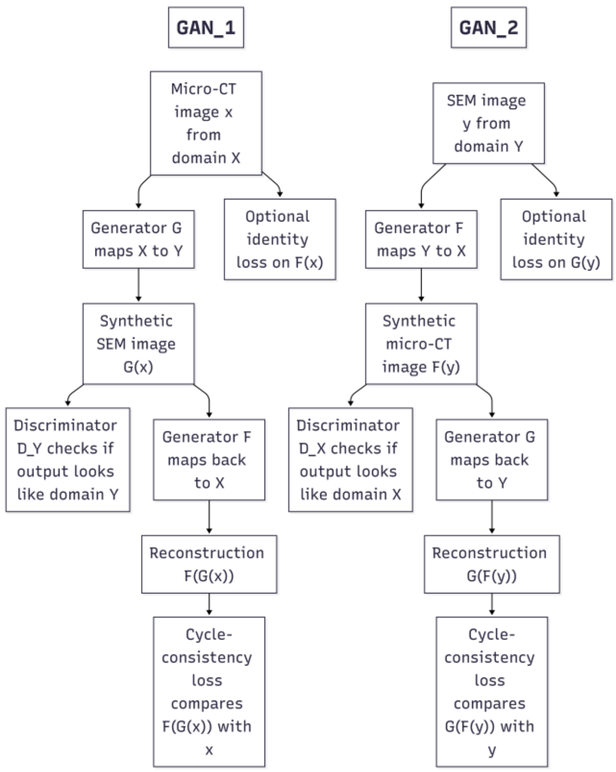

Fig. 2. Flowchart of a Cycle Generative Adversarial Network showing the parallel process for the CycleGAN model 1.

2.3 Super-resolution combined workflow

The combined workflow, illustrated in Fig. 3, for the 3D reconstruction of super-resolved micro-CT images of kaolinite pore-fill microstructures comprised a series of two CycleGAN models, with image-processing operations of interpolation, alignment and/or blending after each. The overall process transformed a starting-state 64×64×64 voxel micro-CT cropped cube of poorly-resolved kaolinite into a final-state 1000×1000×1000 voxel cube, with resolution increase by a factor of 16.

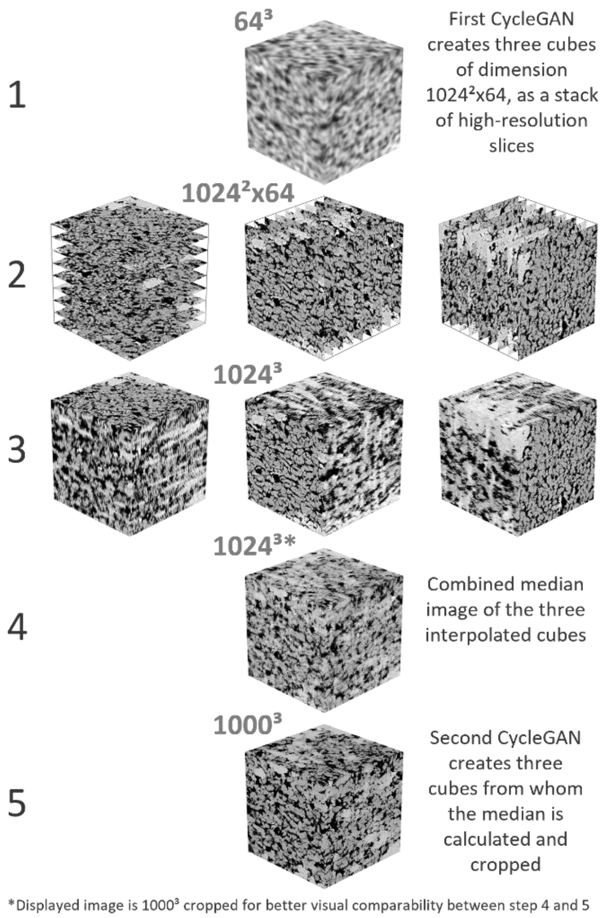

Fig. 3. Simplified illustration of combined workflow to transform a 64^3 micro-CT volume into a super-resolved 1000^3 3D image. In step 1–2, CycleGAN model 1 is applied independently to each plane in the 3 directions to generate 3 high-resolution anisotropic image stacks, then linearly interpolated to isotropic cubes in step 2–3. In step 3–4, the 3 interpolated cubes are spatially aligned and blended by median operation into a single cube. In step 4–5, CycleGAN model 2 is applied as a style-transfer refinement. The final cube is generated by combining the 3 refined cubes using another median-blending operation and subsequent cropping to 1000^3.

In the 1st step (from state 1 to 2 in Fig. 3), the trained CycleGAN model 1 was applied independently to each of the 192 orthogonal planes (XY, XZ, YZ) of the input micro-CT cube, transforming each 64×64 slice into a super-resolved 1024×1024 SEM-like image, thus forming a 1024×1024×64 anisotropic stack in each of the three directions. In Fig. 3, only a subset of the 64 slices of this state 2 stack are shown for clarity. In the 2nd step (from state 2 to 3 in Fig. 3), each of these three stacks was then tri-linearly interpolated separately to give an isotropic 1024×1024×1024 cube. The interpolated slabs of 15 slice thickness in the non-transformed direction between neighboring CycleGAN-transformed slices are naturally less sharp and more disjointed and streaky, owing to the interpolation and spatial inconsistencies between the independent CycleGAN planes.

In the 3rd step (from state 3 to 4 in Fig. 3), these three cubes were combined into a single 1024×1024×1024 cube using a rigid re-alignment of 16 voxels, followed by an element-wise median operation. The blended cube of state 4 in Fig. 3 still contained significant noise and artifacts, remaining from the interpolation and residual mismatches. To address these, the trained CycleGAN model 2 was applied independently to each 1024×1024 slice in each of the three directions of the cube in state 4, which is primarily a style transfer without altering spatial resolution. The 4th step (from state 4 to 5 in Fig. 3) comprised this transformation followed by repeat of the median-blending operation of the 3rd step. Lastly, the resulting blended cube was cropped to 1000×1000×1000 voxels to remove boundary regions affected by the alignments that could not be sufficiently corrected by CycleGAN model 2, giving the final cube in state 5.

2.4 Super-resolution structures and properties

A total of 39 cubes within poorly-resolved kaolinite-rich regions were cropped from the 9 high-resolution micro-CT 3D images, with voxel size 2.33 µm, of the gas reservoir sandstone case study in Section 3. Each cube was processed through the workflow in Fig. 3, resulting in a super-resolved 1000^3 cube with voxel size 0.146 µm. As illustration, representative 2D slices (1000^2) from 5 of these reconstructed kaolinite microstructure cubes are displayed down the left side of Fig. 4. Each such grayscale ML-generated cube was subsequently two-phase segmented (PerGeos software) to separate kaolinite-occupied space from the surrounding resolved pore space. Owing to the consistent image intensities and textures of these ML-cubes, the same segmentation procedure and thresholds could be applied to all 39 cubes, ensuring a comparable basis for the ensuing analysis.

As a first quality-control step, the resolved fractional porosity ϕ_{CG} of each binarized ML-cube was directly compared to the micro-CT grayscale microporosity ϕ_{CT} of its parent cube. Specifically, $\phi_{CT} = (I_s - I_m)/ (I_s - I_p)$, where I_m is the mean grayscale intensity of the cropped cube, and I_p & I_s are the thresholds for resolved pores and quartz grains, respectively, over the full micro-CT image. Figure 4a shows a clear correlation between both porosity measures. Scatter increases as expected for lower-porosity cubes, since denser kaolinite-rich regions in micro-CT have lower grayscale contrast and fewer partially-resolved pore features, also with greater uncertainty in the ϕ_{CT} estimate. Nevertheless, the observed correlation, and the textural consistency between registered micro-CT and super-resolved cube pairs, indicates that the CycleGAN workflow faithfully preserves and enhances the original poorly-resolved microporous regions with realistic SEM-like kaolinite microstructures, rather than generating arbitrary 3D structures. This supports the physical relevance of the ML-cubes and their simulated properties.

On each of the 39 binarized ML-cubes, absolute permeability k was simulated using a Lattice-Boltzmann algorithm (eCore software), and plotted versus the corresponding resolved porosity ϕ_{CG} on semi-log scale in

Fig. 4b. The simulated k ranges over more than two orders of magnitude, from 0.31 to 120 mD, and is very strongly correlated by power law to ϕ_{CG}. For the 5 ML-cube examples at left in Fig. 4, ϕ_{CG} and k decrease progressively from top to bottom, as the microstructures become more tightly packed with kaolinite particles, from relatively loose booklet arrangements to compressed, poorly-connected microporosity. These examples illustrate the range of microstructural variability captured by the workflow, and seen in real SEM images, e.g., Fig. 1c. Even though microporosity presents some of the tighter flow paths through a core plug, the local k of individual reconstructed kaolinite-rich regions can greatly exceed k at plug scale. This plug-scale k is dictated by the effective connectivity of the entire pore system, integrating high-conductivity macro-pores and low-conductivity microporous regions along the tortuous flow paths around the grain framework. The strong porosity-permeability trend in Fig. 4b also results from this lack of macro-pores, grains, laminations and other heterogeneities in the ML-cubes.

For each of the 39 ML-cubes, a pore network model (PNM, eCore software) was extracted for simulation of two-phase flow properties [29,30]. The simulations started with gas-water primary drainage PD from water saturation $S_w = 1$ to its endpoint, followed by water-gas imbibition from this PD endpoint to the S_w of trapped gas. The input pore-scale wettability parameters for imbibition were chosen to be equally strongly water-wet for all cubes, as expected for water-gas.

The output steady-state curves of imbibition relative permeability k_r for all 39 cubes are plotted together in Fig. 4c on linear scale and Fig. 4d on semi-log scale, with red and blue curves denoting gas (k_{rg}) and water (k_{rw}), respectively. In these graphs, S_w at the end of PD and start of imbibition is arbitrarily chosen as 0.1 for all cubes, since this value cannot be specified until the cube flow properties are upscaled to a particular core plug (as in Section 3). The spread of the imbibition k_r curves reflects the variability in pore-space topology and connectivity, and size distribution of pore bodies and throats, across the generated kaolinite microstructures, with gas displaying greater spread in k_r curve shape than water. Mobile saturation range spans from 0.17 to 0.69, while k_{rw} endpoint ranges from 0.01 to 0.55. Lower endpoint values of S_w and k_{rw} generally correspond to tighter, more kaolinite-packed microstructures, suggesting that these regions would have limited contribution to overall system flow, even when they contain connected pore space.

Fig. 4e shows for all 39 cubes the curves of gas-water capillary pressure P_c for PD and imbibition modes, denoted by black and red curves, respectively. The imbibition P_c curves correspond to the k_r simulations (same PNM) shown in Fig. 4c-d, to provide a consistent dataset for further evaluations, and exhibit much less variation in curve shape than for PD.

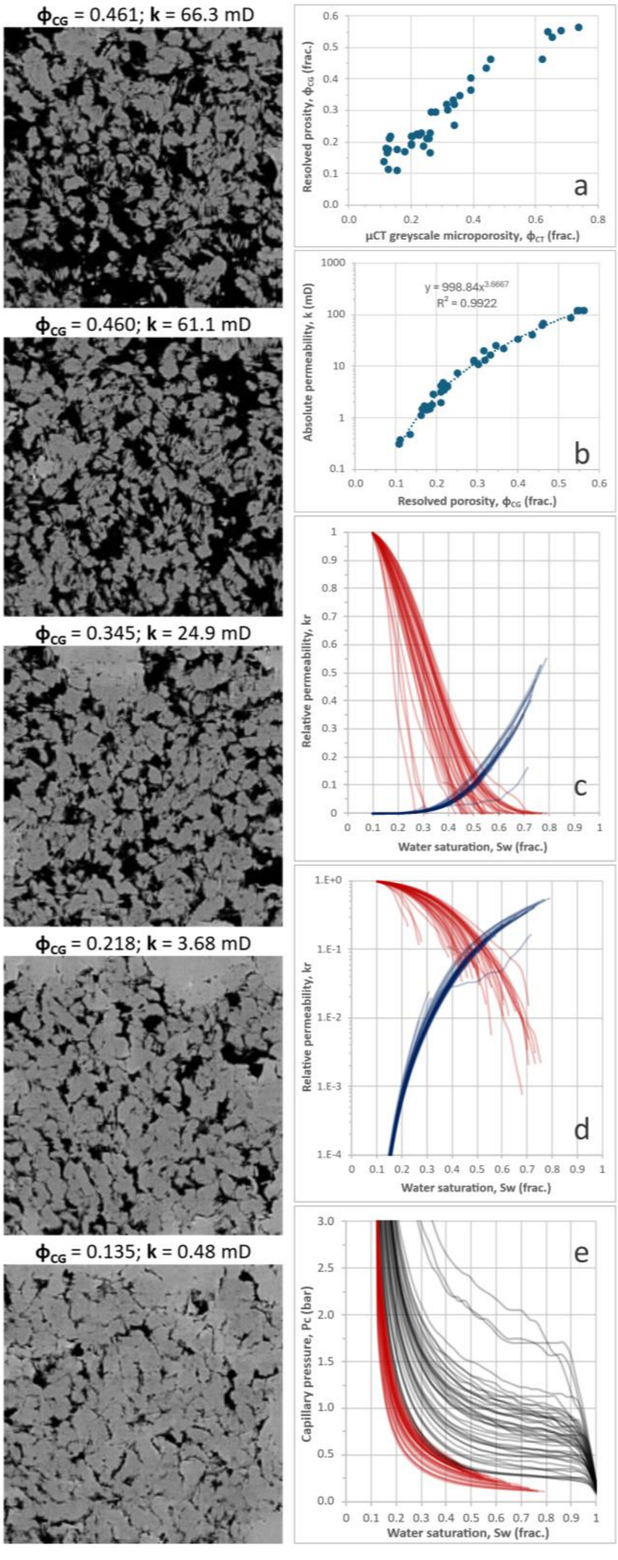

Fig. 4. Left: representative 2D slices (image width 146 µm) of 5 reconstructed super-resolved kaolinite microstructure cubes with varying porosity and permeability. Right: petrophysical and dynamic properties derived from the generated dataset of 39 cubes. (a) CycleGAN-generated porosity vs micro-CT grayscale porosity; (b) simulated absolute permeability vs porosity; (c-d) imbibition relative permeability (red for gas, blue for water) vs water saturation on linear and semi-log scales; (e) capillary pressure vs water saturation, for primary drainage in black and imbibition in red.

3 Case Study

The case study is from an NCS gas field exploration well. The study commenced with non-destructive 3D imaging of 124 clean dry RCA core plugs (horizontal, of diameter 1" and 1.5") by low-resolution micro-CT (HeliScan, 120 kV accelerating voltage). Based on image texture combined with RCA helium porosity ϕ and Klinkenberg-corrected gas permeability k_{Kl}, the plugs were grouped into rock types RT 1-6, where RT 1 to 4 are sandstones with increasing prevalence of thin shale laminations and clays or other cements within the sandstone matrix. The two rock types of lowest reservoir quality are sandy claystones (RT 5) and dense rock (RT 6), while highly heterogeneous plugs, each containing multiple rock types, are denoted RT0. Low-resolution micro-CT images of an example plug (1.5" diameter) from each of RT 1-6 are shown in Fig. 5. The plug images become progressively brighter (denser and less porous) and with lower grain-pore contrast from RT 1 to 6, due to increased filling of the sandstone inter-granular spaces and frequency of shale (bright) laminations.

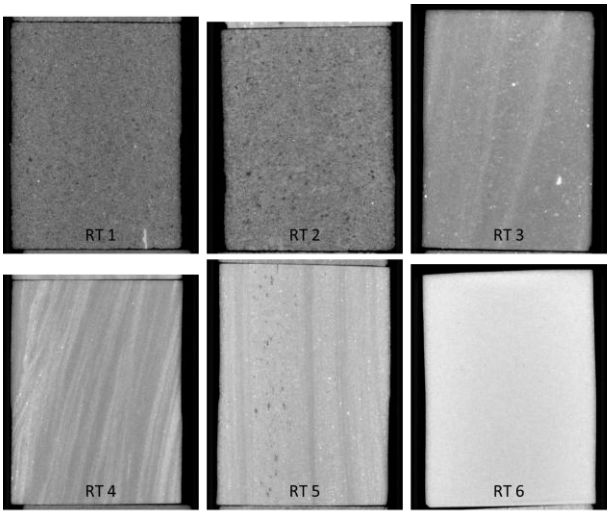

Fig. 5. Central longitudinal slice of low-resolution micro-CT 3D image of 6 plugs (1.5" diameter) representing RT 1-6, with plug image width 43.7 mm and voxel size 34.9 μm.

A subset of 25 plugs from RT 0-6 was selected for a simple SCAL program, including measurement of formation resistivity factor FRF, resistivity index RI from gas-brine PD to irreducible water saturation S_{wi}, and endpoint gas saturation S_{grw} of brine imbibition from S_{wi}. A second subset of 9 plugs from RT 1-4 was selected for DCA on a trim-end, from which one subsample was high-resolution micro-CT 3D imaged and the remaining piece was SEM 2D imaged and mineral mapped.

The cross-plot of lab k_{Kl} vs ϕ in Fig. 6a shows the 25 plugs (1.5" diameter) of RT 0-6 used for SCAL (circle symbols) and the 9 plugs of RT 1-4 used for DCA (triangle symbols), listed in Table 1 in increasing depth order. The two DCA plugs from RT 1 and the three from RT 2 underwent our standard DCA workflow, while our new DCA workflow with ML augmentation was applied to the two plugs from RT 3 and the two from RT 4.

Table 1. Lab-measured porosity and Klinkenberg permeability of 9 plugs A-I of RT 1-4, with standard and new augmented DCA approaches applied (x) to RT 1-2 and 3-4, respectively.

Plug ID	Lab ϕ (frac.)	Lab k_{Kl} (mD)	Image Rock Type RT	DCA Method Standard	DCA Method New
A	0.215	20.7	1	x	
B	0.197	17.0	1	x	
C	0.158	3.90	2	x	
D	0.178	2.33	2	x	
E	0.166	1.30	3		x
F	0.134	0.216	4		x
G	0.202	4.94	2	x	
H	0.148	0.467	3		x
I	0.120	0.145	4		x

3.1 Lab core analysis

The lab-measured S_{wi} of the 25 plugs, from PD by centrifugation to a maximum P_c average of 12.8 bar gas-brine, spanned the range 0.23-0.79 in Fig. 6b, with a strong logarithmic correlation to lab k_{Kl}. Rock types RT 1-2 overlap, while RT 3-5 show a clearer segregation, and the unexpectedly low *Swi* for the one plug from RT 6 has large uncertainty, owing to its very low porosity of 0.035. The corresponding low-resolution micro-CT plug images provide insight into the outlying points. Plugs with S_{wi} lying substantially above the best-fit line have higher-permeability streaks from top to bottom face (e.g. the RT0 plug), while outliers below the line can be due to greater presence of non-porous carbonate cements. The lab S_{wi} trend in Fig. 6b is used to anchor the endpoint of DCA simulations of PD, to account for microporosity below micro-CT resolution and also not fully captured in the ML-generated cubes.

From S_{wi}, the plugs were immersed in brine with all faces open for brine-gas spontaneous imbibition SI with gravimetric measurement of trapped gas saturation S_{grw}. For 4 plugs, SI was followed by centrifuge forced imbibition FI, giving only slight additional gas displacement, thus verifying that the cleaned plugs were water-wetting against gas. The resulting S_{grw} points are plotted vs their corresponding initial gas saturation $S_{gi} = 1 - S_{wi}$ in Fig. 6c. For all plugs, S_{grw} was below 0.31, and well described by Land correlation curve fits for the 90th, 50th and 10th percentiles (Land equation and table of coefficient C values in Fig. 6c), with the exclusion of two plugs with very low $S_{grw} < 0.05$. These lab S_{grw} statistics are later compared to the endpoint of DCA simulations of water-gas imbibition, to confirm that the pore-scale wettability parameters used in the simulations are suitably water-wet.

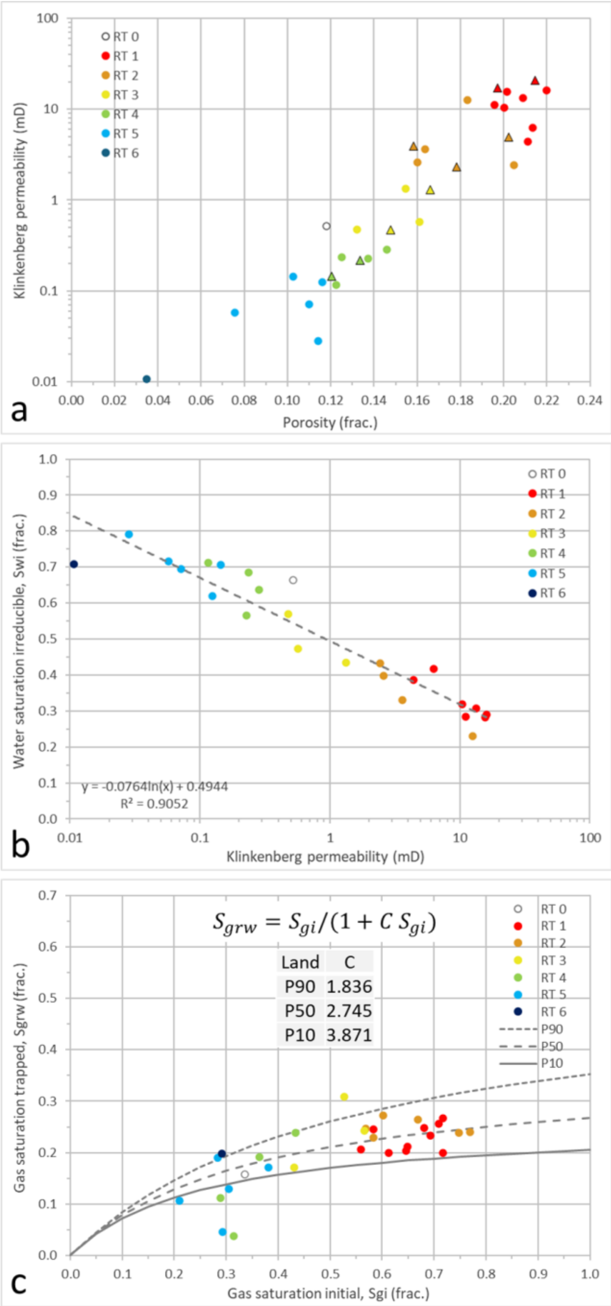

Fig. 6. Lab-measured property cross-plots per rock type for (a) k_{Kl} vs ϕ, with triangle-marked plugs used for DCA and circle-marked plugs used for SCAL in (b) S_{wi} vs k_{Kl}, (c) S_{grw} vs S_{gi}.

3.2 Digital core imaging

For each of the 9 plugs from RT 1-4 for DCA in Table 1, the same rock imaging protocol as illustrated for plug A in Fig. 7 was carried out. From the low-resolution micro-CT plug image in Fig. 7a, a representative trim-end was cut (indicated by the yellow box), from which a sub-plug of 5.5 mm diameter was taken across the plug diameter in direction perpendicular to laminations. The sub-plug was high-resolution micro-CT imaged (HeliScan, 100 kV accelerating voltage) over its full width and most of its height, using a single helical scan with space-filling trajectory and iterative reconstruction, at a voxel size of 2.33 µm (10 times smaller than the low-resolution voxel size) [6]. A central longitudinal slice of the 3D image, of width 5.9 mm and height 18.8 mm, is shown in Fig. 7b, rotated sideways by 90° to fit the page.

From the trim-end remainder, an epoxy-embedded polished section was prepared and carbon-coated for automated acquisition on a SEM system (Scios 2, 20 kV accelerating voltage) of BSE images and EDS maps, using MAPS Mineralogy software, with EDS mineral classification performed by post-processing in NanoMin software [7]. Two such registered image pairs were acquired, namely an overview, covering the full sample cross-section, and a Region-of-Interest ROI, focusing on a square sub-area at higher magnification. Fig. 7c shows the ROI mineral map (4.6 x 4.6 mm) from plug A and colored mineral legend, together with the modal mineralogy of the overview from the 9 DCA plugs. All plugs contain significant fractions of the three clay minerals kaolinite, illite and chlorite, as well as the two mica minerals muscovite and biotite.

3.3 Digital core analysis: Standard approach

For the 5 DCA plugs of RT 1-2 in Table 1, their high-resolution micro-CT sub-plug images resolved sufficient percolating porosity to apply our standard DCA workflow. Each such 3D image was two-phase segmented (PerGeos software) into the corresponding binary image of resolved pore space, from which a vertical stack of 5 cubes, each of side-length 1500 voxels (3.5 mm), was cropped to span the image height (Fig. 7b). Each segmented cropped cube underwent pore-scale simulation of absolute permeability (k, in direction parallel to bedding) by Lattice-Boltzmann algorithm (eCore software). The ratio of simulated k to lab k_{Kl} for the 5 plugs was in the range 0.6-1.3, showing sufficient agreement for the sub-plug cube set to be regarded as representative of the homogeneous parent plug.

A PNM (eCore software) was extracted from each cube, for simulation of PD of water by gas. Sw was linearly rescaled to transform the PD endpoint to the S_{wi} value from the lab trend (Fig. 6b), while maintaining maximum Sw at 1. The PD simulated RI(S_w) curve and Archie saturation exponent n showed good agreement with lab SCAL. Subsequent imbibition of water from S_{wi} to displace/trap gas was simulated on the same PNM for input pore-scale wettability parameters of a water-wet state. The output steady-state curves of water and gas k_r and their P_c were averaged over all 5 cubes of the sub-plug at fixed P_c, then LET [31] fitted for ease of use in dynamic reservoir modelling of aquifer drive. Comparison of simulated imbibition endpoint $S_{wrg} = 1 - S_{grw}$ to its lab trend (Fig. 6c) is discussed later in Fig. 9.

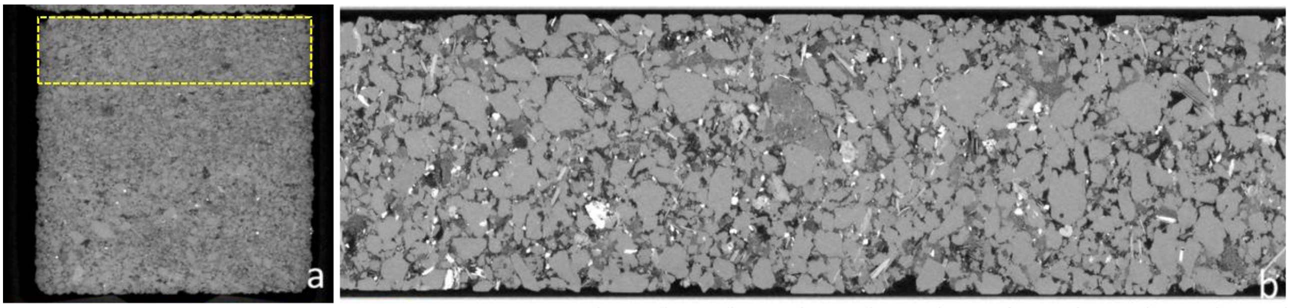

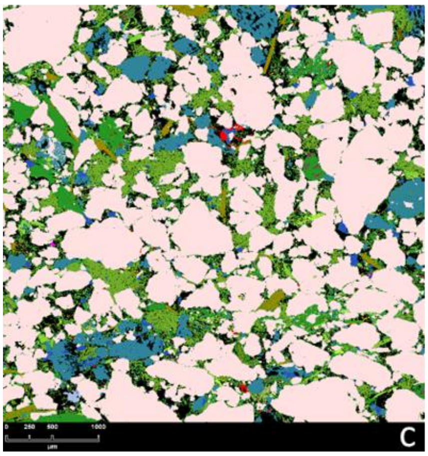

	Plug	A	B	C	D	E	F	G	H	I
Quartz	wt%	67.08	71.66	58.03	50.87	48.99	32.04	51.70	52.71	34.84
*Alkali Feldspar**	wt%	0.08	0.05	0.32	6.52	5.96	5.82	7.48	7.21	4.53
Plagioclase	wt%	9.10	7.14	11.27	9.31	13.18	14.02	11.06	10.58	13.81
*Biotite**	wt%	1.00	1.02	0.86	4.26	3.96	6.19	3.13	1.11	6.54
*Muscovite**	wt%	1.89	1.65	3.14	4.11	3.83	6.67	3.83	4.26	6.53
Kaolinite (Halloysi	wt%	4.94	4.75	9.70	10.63	9.18	12.06	8.48	6.50	10.91
*Illite**	wt%	10.90	10.81	5.44	8.57	8.93	9.87	8.51	9.32	13.95
*Chlorite**	wt%	2.08	0.99	1.92	2.76	2.53	8.10	2.66	2.46	5.88
*Smectites**	wt%	0.26	0.06	0.06	0.07	0.09	0.25	0.07	0.16	0.32
*Zircon**	wt%	0.06	0.02	0.09	0.04	0.12	0.06	0.03	0.09	0.07
*Calcite**	wt%	0.26	0.16	0.27	0.32	0.22	1.13	0.48	0.15	0.15
*Siderite**	wt%	0.07	0.02	0.11	0.52	0.16	0.99	0.07	0.15	0.03
Dolomite	wt%	0.54	0.37	3.89	0.11	0.07	0.27	0.09	1.57	0.07
*Ankerite**	wt%	0.64	0.44	3.70	0.16	0.11	0.39	0.15	1.55	0.11
Apatite	wt%	0.25	0.10	0.04	0.05	0.08	0.08	0.12	0.62	0.14
Monazite	wt%	0.06	0.09	0.09	0.10	0.11	0.04	0.10	0.00	0.03
Pyrite	wt%	0.26	0.36	0.30	0.93	1.30	1.18	1.47	0.93	1.00
Gypsum/Anhydrite	wt%	0.00	0.00	0.00	0.00	0.00	0.00	0.00	0.00	0.01
Barite	wt%	0.01	0.00	0.01	0.00	0.00	0.00	0.01	0.05	0.01
Rutile	wt%	0.53	0.32	0.76	0.66	1.17	0.84	0.55	0.59	1.06

Fig. 7. Central longitudinal slice of micro-CT 3D image of (a) plug A, with image width 29.7 mm and voxel size 23.7 µm, and (b) its sub-plug, with image width (height) 5.9 mm and voxel size 2.33 µm, together with (c) SEM 2D mineral map ROI from its polished section, with image width 4.6 mm and EDS pixel size 6.0 µm, and table of overall EDS mineral composition from all 9 DCA plugs.

3.4 Digital core analysis: Augmented approach

For the 4 plugs of RT 3-4 in Table 1, with k_{Kl} range 0.1-1 mD, their high-resolution micro-CT sub-plug images resolved insufficient percolating porosity for simulation of water-gas flow properties using our standard DCA approach. While a smaller sub-plug (e.g. 3 mm diameter) would improve micro-CT resolution (to 1.3 µm), this reduced voxel size would still not suffice, and lead to unrepresentatively small simulation cubes. For this reason, our new DCA workflow, involving augmentation of the high-resolution micro-CT 3D image with ML-generated clay microstructure 3D images/properties from Section 2.4, was applied to these 4 tightest plugs. Although the plugs contain a mix of clay minerals (Fig. 7c table), their inter-granular microporosity relevant to gas flow is predominately hosted by kaolinite booklet aggregates (e.g., Fig. 1c for plug *E*), so the ML-generated cubes from Section 2.4 are suitable for application, as outlined below.

For each of these 4 DCA plugs of RT 3-4, its high-resolution micro-CT image was three-phase segmented (PerGeos software) into resolved pores, solid grains and the intermediate phase of sub-resolution microporous regions. The micro-CT grayscale intensity field I_m within the intermediate phase was linearly rescaled to grayscale microporosity field ϕ_{CT}, as described in Section 2.4. The mean and plus/minus 0.5 and 1 standard deviation of the grayscale microporosity histogram were then calculated.

From the library of 39 ML-generated 1000-voxel cubes with simulated flow properties in Section 2.4, the 5 cubes with ϕ_{CT} closest-matching these 5 histogram values were selected. For the example of plug *E*, these 5 chosen cubes were those shown in the images at left in Fig. 4, together with their segmented porosity ϕ_{CG} (i.e. porosity at the super-resolution of 0.146 µm) and simulated *k*. The 5 corresponding PNM-simulated k_{rg} & k_{rw} curve pairs for PD and imbibition (the latter from Fig. 4c-d) were then combined at fixed P_c (from Fig. 4e), and upscaled to the three-phase segmented high-resolution micro-CT 3D image. PD endpoint S_{wi} was linearly transformed to its lab-trend value in Fig. 6b, as for the standard DCA workflow.

These simulated k_r curves of the 4 DCA plugs of RT 3-4 for water-gas imbibition from the lab-anchored S_{wi} are shown as semi-log plots in Fig. 8, together with their LET fits, for RT 3 (plugs *E* & *H*) in the top row and RT 4 (plugs *F* & *I*) in the bottom row. The graphs also show in vertical lines the P90, P50, P10 values of endpoint S_{wrg} from the Land fits to lab data (Fig. 6c), evaluated at the lab-fitted S_{wi} value for plug k_{Kl} (Fig. 6b). As expected, the k_r curves are highly compressed by the high S_{wi}, and increasingly so with decreasing k_{Kl} from plug *E* to *H* to *F* to *I*. The k_r cross-over shifts increasingly closer to the endpoint S_{wrg}, which lies in the vicinity of the lab-fitted P50 value for all 4 plugs in Fig.8.

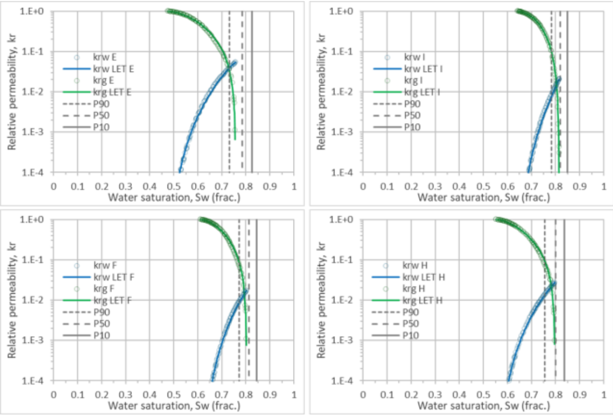

Fig. 8. Simulated water-gas imbibition k_r vs S_w (unfilled circles) and LET curve fits for the 4 DCA plugs of RT 3-4 as semi-log plots.

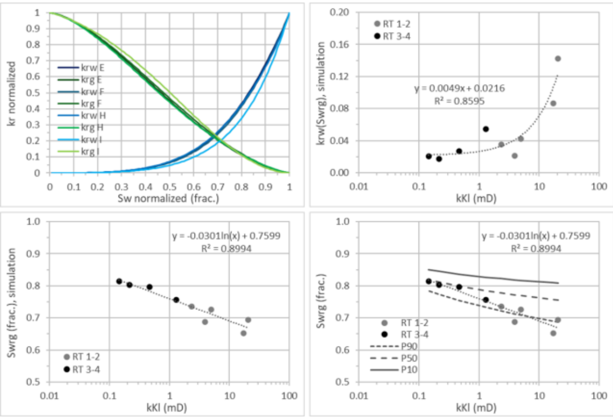

Fig. 9. (a) Simulated water-gas imbibition LET curves of normalized k_r vs normalized S_w for the 4 DCA plugs of RT 3-4 as linear plots, together with simulated imbibition endpoint (b) k_{rw} and (c) S_{wrg} vs lab k_{Kl} for all 9 DCA plugs, combined in (d) with lab-derived curves for P90, P50 & P10 S_{wrg}.

Related information is provided in Fig. 9, including the plot of imbibition LET normalized k_r versus normalized S_w in Fig. 9a. Curve shape and LET parameters are almost identical for 3 of the 4 plugs, while the lowest permeability plug *I* deviates somewhat. Further analysis of imbibition endpoint is given in Fig. 9b-d, combining the simulation results for the 4 DCA plugs of RT 3-4 using the augmented workflow with the 5 DCA plugs of RT 1-2 using the standard workflow. Figure 9b shows a weak correlation of increasing simulation endpoint k_{rw} to increasing lab k_{Kl} across the 9 plugs, with reasonable consistency between the lower and higher permeability plugs of the two DCA approaches. Figure 9c displays a stronger correlation of decreasing simulation endpoint S_{wrg} (i.e. increasing gas trapping) to increasing lab k_{Kl} across the 9 plugs, again with consistency between the two approaches. Figure 9d adds to these simulation points the above-mentioned lab-derived curves for P90, P50 & P10 S_{wrg}, showing that the predicted simulation endpoint S_{wrg} is close to its lab-fitted P50 for RT 3-4 (as seen in Fig. 8), while RT 1-2 lie near to, or even below, the lab-fitted P90. The augmented DCA approach thus gives results in line with the standard approach, possibly with a more accurate representation of gas trapping.

4 Conclusions

This paper demonstrated a machine-learning workflow for the 3D reconstruction of super-resolved micro-CT images of kaolinite-rich microporous regions in NCS sandstones, which honors the textures in high-resolution SEM 2D images of polished sections. Two trained CycleGAN models, combined with interpolation, alignment, median blending and final cropping operations, were applied in series to upscale 64^3 voxel micro-CT real input volumes of poorly-resolved kaolinite particle aggregates with voxel size of 2.33 µm into 1000^3 voxel super-resolved synthetic volumes with voxel size of 0.146 µm. A total of 39 such cubes were generated, providing a library from which suitable candidates can be chosen for use in augmented digital core analysis workflows.

For each cube, the transformation preserved the spatial distribution of grayscale intensities in the input micro-CT, while refining it with realistic kaolinite-booklet shapes, edges and junctions, and removing almost all of the artifacts from spatial and directional mismatches during the process. After this confirmation of visual similarity, the super-resolved cube underwent binary segmentation of pore space for a suite of quantitative analyses relevant to fluid flow. The correlation between calculated porosity of input micro-CT cube and corresponding super-resolved cube further demonstrated the textural fidelity and provides a direct means to select members from the set of 39 to best represent the micro-CT microporosity of a given sandstone sample. Assignment of corresponding flow properties then follows unambiguously from the simulated absolute permeability and pore-network modeled water-gas relative permeabilities and capillary pressure of the super-resolved cube.

The case study from a NCS gas exploration well illustrated the extension from standard digital core analysis workflow, for sandstone rock types with sufficient resolved percolating porosity, to the augmented workflow for tighter, more clay-rich rock types. For the latter, 5 super-resolution cubes were selected to represent the microporosity distribution of each sample, from which upscaled water-gas dynamic properties were calculated. Regarding imbibition, the simulated trapped gas saturations were consistent with laboratory-derived trends, and endpoint water relative permeability was consistent with simulation results from the more permeable rock types. In future work, the cubes will be integrated into a more-developed multiscale simulation framework, for coupling flow between micro-CT resolved pores and super-resolved microporosity.

The authors acknowledge the contribution of intern Jeffy Elson to machine-learning coding, and thank Harbour Energy and our partners AkerBP AS, Orlen Upstream Norway AS and Petoro AS for permission to publish.

References

1. V. Cnudde, M.N. Boone, *Earth-Sci. Rev.*, **123**, 1–17 (2013)
2. T. Bultreys, W. De Boever, V. Cnudde, *Earth-Sci. Rev.*, **155**, 93–128 (2016)
3. N. Saxena, A. Hows, R. Hofmann, F.O. Alpak, J. Freeman, S. Hunter, M. Appel, *Adv. Water Resour.*, **116**, 127–144 (2018)
4. N. Saxena, A. Hows, R. Hofmann, F.O. Alpak, J. Dietderich, M. Appel, J. Freeman, H. De Jong, *Adv. Water Resour.*, **134**, 103419 (2019)
5. M.J. Blunt, *Multiphase Flow in Permeable Media: A Pore-Scale Perspective* (Cambridge University Press, Cambridge, 2017)
6. A. Sheppard, S. Latham, J. Middleton, A. Kingston, G. Myers, T. Varslot, A. Fogden, T. Sawkins, R. Cruikshank, M. Saadatfar, N. Francois, C. Arns, T. Senden, *Nucl. Instrum. Methods Phys. Res. B*, **324**, 49–56 (2014)
7. S. Han, S.C. Löhr, A.N. Abbott, A. Baldermann, J. Farkaš, W. McMahon, K.L. Milliken, M. Rafiei, C. Wheeler, M. Owen, *Front. Earth Sci.*, **10**, 956912 (2022)
8. L.C. Ruspini, G. Lindkvist, S. Bakke, L. Alberts, A.M. Carnerup, P.E. Øren, in *SPE Low Perm Symp.*, SPE-180268-MS (2016)
9. L.C. Ruspini, P.E. Øren, S. Berg, S. Masalmeh, T. Bultreys, C. Taberner, T. Sorop, F. Marcelis, M. Appel, J. Freeman, O.B. Wilson, *Transp. Porous Media*, **139**, 301–325 (2021)
10. S. Foroughi, B. Bijeljic, Y. Gao, M.J. Blunt, *Water Resour. Res.*, **60**, e2023WR036393 (2024)
11. P.E. Øren, S. Bakke, *Transp. Porous Media*, **46**, 311–343 (2002)
12. K. Wu, M.I.J. Van Dijke, G.D. Couples, Z. Jiang, J. Ma, K.S. Sorbie, J. Crawford, I. Young, X. Zhang, *Transp. Porous Media*, **65**, 443–467 (2006)
13. L. Mosser, O. Dubrule, M.J. Blunt, *Phys. Rev. E*, **96**, 043309 (2017)
14. L. Mosser, O. Dubrule, M.J. Blunt, *Transp. Porous Media*, **125**, 81–103 (2018)
15. D. Volkhonskiy, E. Muravleva, O. Sudakov, D. Orlov, E. Burnaev, D. Koroteev, B. Belozerov, V. Krutko, *Phys. Rev. E*, **105**, 025304 (2022)
16. J. Feng, Q. Teng, B. Li, X. He, H. Chen, Y. Li, *Comput. Methods Appl. Mech. Eng.*, **368**, 113043 (2020)
17. Y. Yang, F. Liu, J. Yao, S. Iglauer, M. Sajjadi, K. Zhang, H. Sun, L. Zhang, J. Zhong, V. Lisitsa, J. *Nat. Gas Sci. Eng.*, **99**, 104411 (2022)
18. H. Amiri, H. Vogel, O. Plümper, J. Geophys. Res. *Mach. Learn. Comput.*, **1**, e2024JH000178 (2024)
19. Y.D. Wang, R.T. Armstrong, P. Mostaghimi, *J. Pet. Sci. Eng.*, **182**, 106261 (2019)
20. Y.D. Wang, R.T. Armstrong, P. Mostaghimi, *Water Resour. Res.*, **56**, e2019WR026052 (2020)
21. H. Chen, X. He, Q. Teng, R.E. Sheriff, J. Feng, S. Xiong, *Phys. Rev. E*, **101**, 023305 (2020)
22. Y. Niu, Y.D. Wang, P. Mostaghimi, P. Swietojanski, R.T. Armstrong, *Geophys. Res. Lett.*, **47**, e2020GL089029 (2020)
23. Y. Niu, Y.D. Wang, P. Mostaghimi, J.E. McClure, J. Yin, R.T. Armstrong, *Phys. Rev. Appl.*, **15**, 064033 (2021)
24. Y. Niu, S.J. Jackson, N. Alqahtani, et al., *Transp. Porous Media*, **144**, 825–847 (2022)
25. M. Bizhani, O.H. Ardakani, E. Little, *Sci. Rep.*, **12**, 4264 (2022)
26. I. Goodfellow, J. Pouget-Abadie, M. Mirza, B. Xu, D. Warde-Farley, S. Ozair, A. Courville, Y. Bengio, *Adv. Neural Inf. Process. Syst.*, **27** (2014)
27. A. Radford, L. Metz, S. Chintala, arXiv:1511.06434 (2015)
28. J.Y. Zhu, T. Park, P. Isola, A.A. Efros, in Proc. *IEEE Int. Conf. Comput. Vis.*, 2223–2232 (2017)
29. S. Bakke, P.E. Øren, *SPE J.*, **2**, 136–149 (1997)
30. P.H. Valvatne, M.J. Blunt, *Water Resour. Res.*, **40**, W07406 (2004)
31. F. Lomeland, E. Ebeltoft, W.H. Thomas, in *Int. Symp. Soc. Core Analysts*, SCA2005-32 (2005)